Investigation of optoelectronic properties of spin-coated SnO₂/Al₂O₃ nanoflower thin film

R. MAHANTA[1], P. CHETRI[1,*], K. C. HANDIQUE[2]
[1]Department of Physics, Debraj Roy College (Autonomous), Golaghat 785621, Golaghat, Assam, India
[2]Department of Physics, Jengraimukh College, Majuli 785105, Assam, India

In this work, three thin films of pure SnO₂ and pure Al₂O₃ and SnO₂/Al₂O₃ composite are synthesized via sol-gel-assisted spin coating technique. The UV-Visible absorbance, transmittance, and reflectance measurements of these films are analysed to determine their optical properties. An X-ray diffractometer (XRD), scanning electron microscope (SEM), and Fourier transform infrared (FTIR) spectrometer are also used to investigate the structural characteristics of these spin-coated films. SEM images demonstrate the formation of nanoflowers in SnO₂/Al₂O₃ thin film. I-V characterization reveals that pure SnO₂ and Al₂O₃ films exhibit ohmic characteristics but their composite counterpart i.e. SnO₂/Al₂O₃ film demonstrates non-ohmic characteristics.

1. Introduction

In modern times, the growing human population has resulted in an increase in energy consumption as a result of the use of technology in every possible field. It is predicted that the global energy demand will increase by three times by 2050. In order to meet this energy demand, researchers are focused on developing alternative and renewable energy sources [1,2]. In recent times, utilization of the abundant energy of the sun is considered one of the most efficient ways to tackle the energy crisis faced by modern society. To achieve this goal, modern research has considered optoelectronic technology as one of the prominent and emerging technology [3]. In addition, cost-effective and highly efficient devices such as photodiodes [4], light emitting diodes (LEDs) [5], field effect transistors (FETs) [6], solar cells [7], transparent conductors [8] etc. are synthesized by using this technology to replace their conventional counterparts. By producing green and renewable energy, optoelectronic devices like solar cell [7] reduces the growing consumption of fossil fuels. So, these devices draw researchers' attention to achieving a pollution-free world by reducing carbon emissions.

Metal-oxides are frequently used in a variety of applications-based domains in the present research due to their tunable optical bandgap and outstanding chemical and mechanical properties [9-12]. Metal oxides can be doped with foreign atoms [13-15] and combined with other metal oxides [16-18] to form heterostructures with improved optical and electrical characteristics. As technology advances, metal-oxide-based materials are synthesised in a variety of forms, including thin films, nanoparticles, nanoflowers, nanorods, etc. They display diverse characteristics depending on their form, and as a result, they are frequently used in catalysis [19], optoelectronics [20], energy harvesting [21], and storage devices [22]. Metal-oxide thin films are extremely valuable due to their dual properties: they allow light to transmit through them and conduct electricity like metals [23,24]. In recent times, a lot of optoelectronic devices are constructed with thin metal-oxide films like SnO₂, CuO, ZnO, NiO, MoO₃ etc. Much work has been done to explore the functionalities of these metal oxides by preparing optoelectronic devices such as thin-film transistors (TFTs), light-emitting diodes (LEDs), and solar cells. To achieve the desired characteristics, these devices rely on efficient charge transport and injection. By engineering the composition or configuration of these metal oxide thin films, the electrical properties of these thin films can also be tailored [25-27].

SnO₂ is a multifunctional IV-VI metal-oxide semiconductor that finds application in various application fields due to its exotic electrical and optical properties [28]. At room temperature, bulk SnO₂ exhibits a wide bandgap of 3.6-4 eV and due to this wide bandgap, it can absorb light mainly in the UV region [28]. However, the bandgap of SnO₂ can be tuned to a desired value by changing its particle size into a nano range and controlling its synthesis parameters in various synthesis routes. As a result, excellent electronic properties like high electron mobility and affinity, and good conductivity of nano-sized SnO₂ make it a good choice for different optoelectronic and sensor devices [29]. In addition, SnO₂ nanoparticles also possess resistance towards high temperatures, chemical inertness, mechanical hardness and non-toxic behaviours. Therefore, in recent times, SnO₂ nanoparticles are considered a good synthesis material for the fabrication of various optoelectronic devices. A variety of metals such as Ag [13], F [30], Ni [30], Mg [14], Ba [31], Eu [31] etc.

are doped with SnO_2 and metal-oxides such as ZnO [32], TiO_2 [17] etc. are coupled with SnO_2 to prepare highly efficient thin films and they are employed to address a variety of issues faced by today's world.

In modern times, many traditional methods such as electron beam evaporation, dip coating, chemical beam evaporation, chemical vapour deposition, physical vapour deposition, Spray pyrolysis etc. are widely employed for the synthesis of thin films. The spin-coating film synthesis technique offers more advantages than the above-mentioned methods and hence attracts the attention of scientists. Using the spin-coating technique, highly efficient thin films can be synthesised in a very cost-effective way and this easy film synthesis technique offers good control over the physical and chemical properties of the synthesized films. Moreover, it is a simple way to precisely control the doping ratio and ensure constant element dispersion inside the film. This approach greatly assists in changing the microstructure, optical properties, and electrical behaviours of the film [33,34].

The novelty of our study lies in the development of SnO_2/Al_2O_3 composite films with a unique nano-flower morphology and non-ohmic electrical behaviour, combining the advantages of both components while introducing new functionalities due to the heterojunction between SnO_2 and Al_2O_3. While pure SnO_2 films have been widely studied for their optoelectronic properties, they often suffer from poor conductivity and surface defects, limiting their performance in applications like sensors, photovoltaic and photocatalysis [35]. Similarly, Al_2O_3 films, while stable and offering a wide bandgap, lack sufficient conductivity for many applications [36,37]. Our composite material, with its enhanced surface area and improved charge transport properties, is more suitable for electronic and optoelectronic applications than traditional thin films or nanoparticles [38,39]. The nano-flower morphology increases the surface area, which is crucial for photocatalysis and sensors [40], and the incorporation of Al_2O_3 in the SnO_2 matrix affects crystallization and electronic behaviour by inhibiting grain growth, leading to finer grains in the composite films [41]. The non-ohmic electrical behaviour observed in the SnO_2/Al_2O_3 composite, attributed to the heterojunction between the two materials, makes it a potential candidate for rectifying devices, photodetectors, and other optoelectronic applications. This behaviour, which contrasts with the ohmic behaviour typically seen in pure SnO_2 films, is explained by the energy band alignment between SnO_2 and Al_2O_3, leading to enhanced charge transfer at the interface. Our films also show a lower turn-on voltage and higher current density compared to pure SnO_2 films, suggesting promising device applications. The localized states at the heterojunction significantly impact charge transport and recombination dynamics, contributing to the non-ohmic behaviour [42]. This finding aligns with previous studies on other composite systems but is distinct for SnO_2/Al_2O_3, highlighting its potential in applications requiring rectifying properties or high-sensitivity sensor devices. Our work presents a novel SnO_2/Al_2O_3 composite film prepared using a sol-gel assisted spin-coating

technique that improves upon the individual properties of SnO_2 and Al_2O_3, offering new functionalities for optoelectronic and sensor applications, and contributes to the growing body of research on composite materials and heterojunctions for next-generation electronic and photocatalytic devices.

Here, we want to investigate the influence of Al_2O_3 on the optoelectronic properties of SnO_2 film. Until now, very low numbers of literature are found related to the study of properties and optoelectronic applications of SnO_2/Al_2O_3 heterojunctions. Al_2O_3 possesses dielectric behaviour with a wide bandgap in its bulk state [43,44]. Converting bulk Al_2O_3 into the nano range by adopting some changes in its synthesis routes can impart high influence on its bandgap and hence on its electrical conductivity. In addition, high thermal and chemical stability, high surface area, excellent mechanical strength and non-toxic behaviours [45] motivate us to study the influence of Al_2O_3 nanoparticles on the optical, structural and optoelectronic properties of SnO_2 thin film. To have a clear understanding of the effect of Al_2O_3 nanoparticles on SnO_2 thin film, two additional thin films of pure SnO_2 and Al_2O_3 are also prepared under identical conditions and their properties are compared with the SnO_2/Al_2O_3 composite film. This film with enhanced optical, structural and optoelectronic properties can provide us with a new efficient material which can find high applications for the fabrication of various optoelectronic devices like photodiodes, solar-cells, LEDs, etc.

2. Experimental

2.1. Synthesis of SnO_2 solution

Synthesis of the SnO_2 solution started with the mixing of 2 gm of $SnCl_2.2H_2O$ with 22 ml deionized water and 10 ml ethanol. The mixer is then stirred for 5 minutes at 80^0 C. Then, 2 ml of concentrated HCl is added to the above-mentioned solution in a dropwise manner with the help of a pipette. This addition of HCl is done very slowly and the whole process takes 15 minutes under constant stirring at 80 °C. Finally, the pH of the solution is fixed at 8 by the addition of the suitable amount of ammonia. A white SnO_2 is obtained and stored in a beaker for the next process [46].

2.2. Synthesis of Al_2O_3 solution

For the synthesis of the Al_2O_3 solution, we take $Al_2(SO_4)_3$ as a precursor. Initially, 4 gm $Al_2(SO_4)_3$ is mixed with 44 ml deionized water and the solution is stirred for 5 minutes at 80 °C. After that, 20 ml of aqueous ammonia (35%) is added dropwise to the solution under same the stirring speed for 30 minutes at the same temperature. An off-white solution is formed and the solution is kept in a beaker [47].

2.3. Synthesis of SnO_2/Al_2O_3 solution

To prepare a composite solution of SnO_2 and Al_2O_3, we repeat the above two processes once again and mixed

with the help of a magnetic stirrer at room temperature. After 15 minutes of stirring, we obtain a grey-coloured solution and the solution is kept in a beaker [47].

2.4. Synthesis of spin coated SnO₂, Al₂O₃ and SnO₂/Al₂O₃ films

Spin coating is a very promising technique used to prepare films with desirable thicknesses on a flat substrate. In the spin coating technique, a small amount of the sample solution is applied to the centre of the substrate. Then the spin coater rotates the substrate at around 10,000 rpm and under the action of centrifugal force, the sample solution is spread out on the substrate. Due to the spinning off excess coating material, we obtain films with suitable thickness [48,49]. In our case, we use 2×2 cm² glass slides as substrates. After mounting the glass substrate on the spin coater, a small puddle (2 ml) of coating material is applied to the centre of the substrate with a dropper. Then, the substrate is rotated at 2500 revolutions per minute for 2 minutes. During this stage, all the excess coating material moves away due to the action of centrifugal force. A layer of coating material is deposited on the glass substrate. The prepared one-layer film is dried at 80 °C for 10 minutes. The glass substrate is then remounted to the spin coater for deposition of the next layer of coating material. This is done by repeating the same process. Six layers of coating material are deposited on the glass substrate using the same process. By taking pure SnO₂, pure Al₂O₃ and composite SnO₂/Al₂O₃ solutions as coating material, we have synthesized six layered spin-coated films of SnO₂, Al₂O₃ and SnO₂/Al₂O₃ separately by adopting the above-mentioned procedure under the same rpm of the spin coater with identical time and temperature conditions. The diagrammatic representation of the film synthesis process is depicted in Fig. 1.
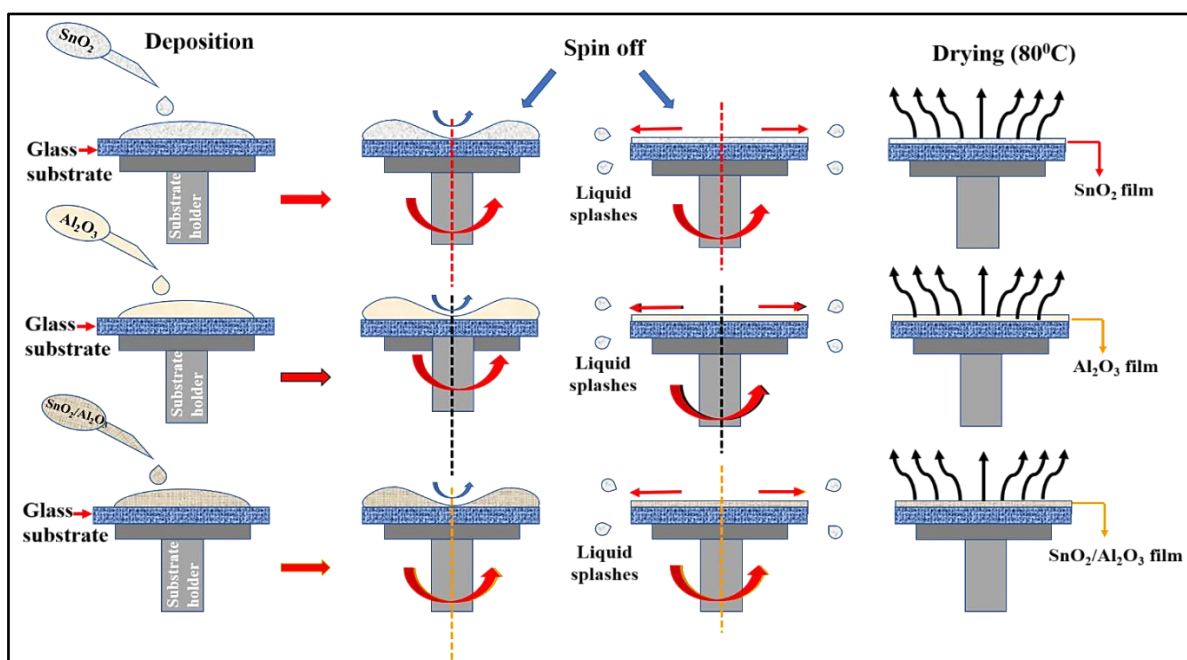

Fig. 1. Diagrammatic representation of film synthesis by spin-coating method (colour online)

3. Details of film characterization

To study the optical characteristics of the films, absorbance, transmittance and reflectance spectra are recorded in a Shimadzu-1900 UV-Visible Spectro-photometer. To investigate the structural properties of these films a Rigaku Ultima-4 x-ray diffractometer is used. This x-ray diffractometer has intense CuKα radiation of 1.54 Å wavelength and operates at a scanning speed of 10 per minute. We have calculated the crystallite size and microstrain of our films by analysing the data obtained from the XRD spectrum. Moreover, to have a clear idea about the functional groups of our films we have also recorded the FTIR spectrum in transmittance mode with an Agilent Cary 630 Fourier Transform Infrared Spectrometer. In order to gain knowledge about the surface morphology of our films, we have captured FESEM images of these films with a Zeiss, Sigma Field emission scanning electron microscope. Finally, the I-V characteristics of these films are studied with a Keithley source meter (Model: Keithley 2450).

4. Results and discussions

4.1. Study of structural properties

X-ray diffraction patterns of pure SnO₂, pure Al₂O₃ and SnO₂/Al₂O₃ films are displayed in Fig. 2 (a), (b) and (c) respectively. It is clear from the figure that pure SnO₂ and SnO₂/Al₂O₃ films exhibit semicrystalline nature while pure Al₂O₃ film shows amorphous nature. In this figure the diffraction peaks corresponding to the lattice planes of SnO₂ are presented by the '*' and that of Al₂O₃ are denoted by the '#' symbol respectively. Diffraction peaks of SnO₂ are validated by reference JCPDS: 41-1445 and

the tetragonal structure of SnO_2 is observed. Similarly, diffraction peaks of Al_2O_3 are confirmed by JCPDS: 88-0107. Fig. 2 (c) represents a mixed XRD pattern of SnO_2 and Al_2O_3 with SnO_2 as the main phase along with feeble peaks of Al_2O_3. Therefore, the existence of both SnO_2 and

Al_2O_3 peaks confirms the formation of the composite structure of SnO_2/Al_2O_3. In this heterostructure, SnO_2 exhibits strong XRD peaks whereas Al_2O_3 exhibits relatively weak XRD peaks [50].
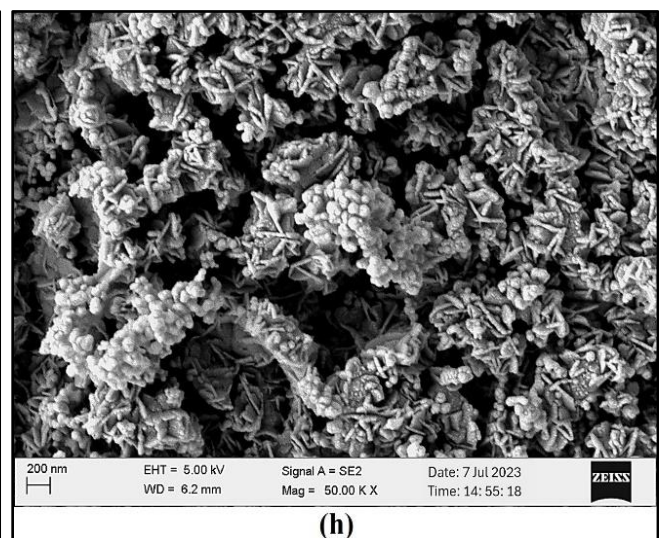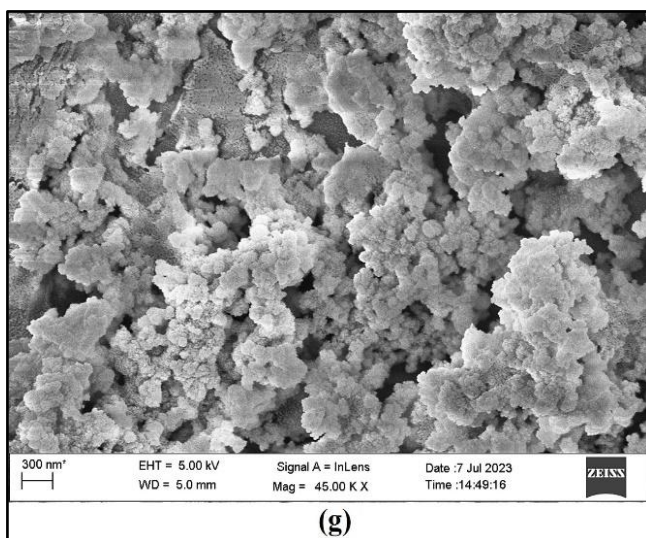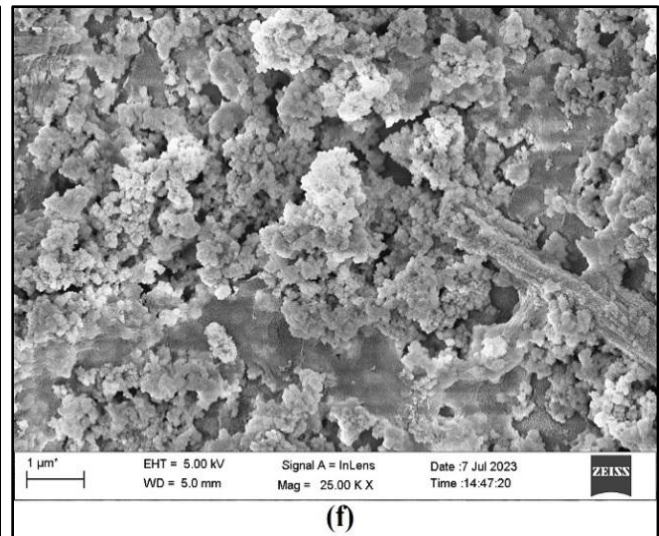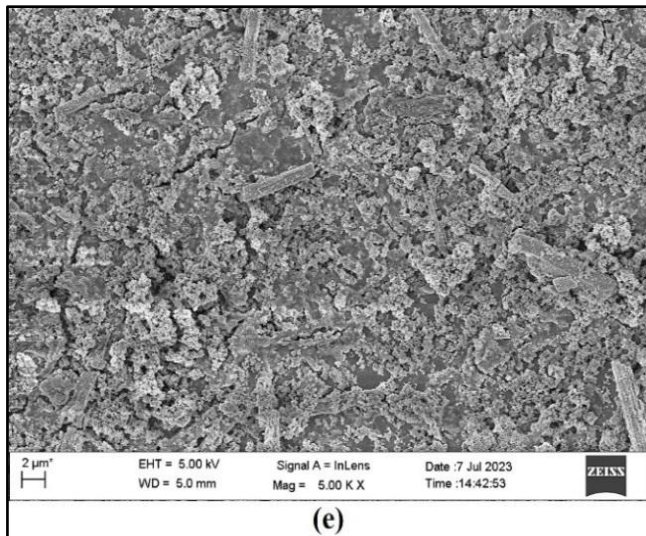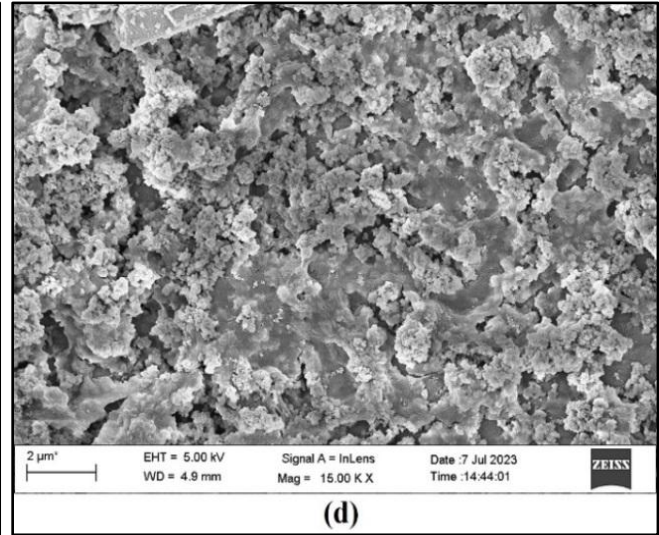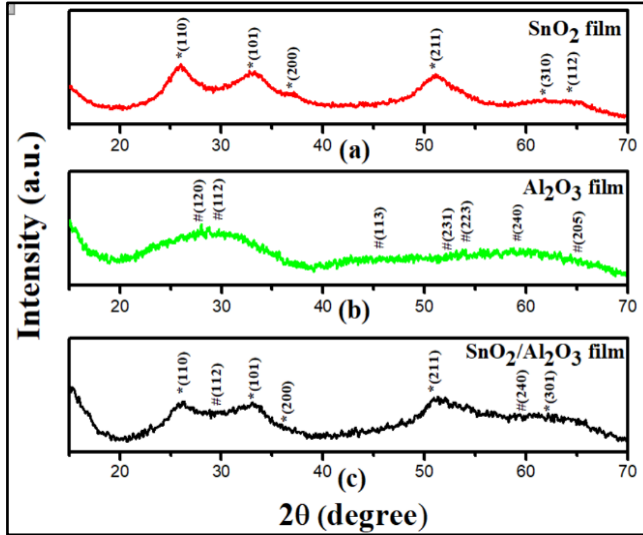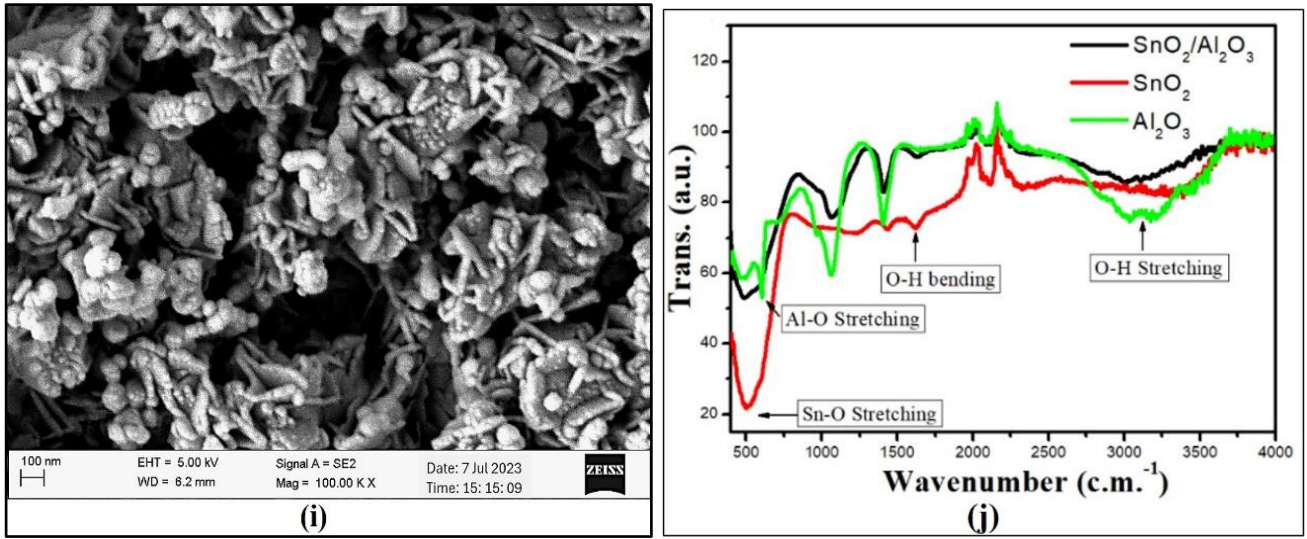
Fig. 2. X-ray diffraction pattern of (a) SnO₂, (b) Al₂O₃ and (c) SnO₂/ Al₂O₃ films. FESEM images of (d) SnO₂ film (e) Al₂O₃ film, (f) low resolution SnO₂/ Al₂O₃ film and (g) High resolution SnO₂/ Al₂O₃ film (300 nm), (h) High resolution images of nanoflower morphology of SnO₂/ Al₂O₃ film (200 nm), (i) High resolution images of nanoflower morphology of SnO₂/ Al₂O₃ film (100 nm) and (j) FTIR transmission spectra of SnO₂, Al₂O₃ and SnO₂/Al₂O₃ films (colour online)

Crystallite sizes of SnO₂, Al₂O₃ and SnO₂/Al₂O₃ are calculated from both the Scherrer formula and Williamson-Hall plot, respectively. Williamson-Hall plot is considered because it is a very sophisticated method from which lattice strain can be calculated. The difference in crystallite size obtained from these two approaches can reveal many important information about our spin-coated films [51]. To calculate the crystallite sizes of our films using the Scherrer formula, the equation (1) is used,

$$D = \frac{k\lambda}{\beta cos\theta} \qquad (1)$$

Here, 'D', 'λ', 'β' and 'θ' are crystallite size, wavelength of X-ray (1.54 Å), full wave half maxima (FWHM) and Braggs angle, respectively. 'k' is dimensionless constant with value 0.91 [51].

Table 1. Crystallite size and lattice strain of the films calculated using Scherrer formula and W-H plot

Name of films	Crystallite size in nm		Lattice strain
	Scherrer formula	W-H plot	
SnO₂	4.78	11	0.0137
Al₂O₃	0.46	1.24	0.1427
SnO₂/Al₂O₃	4.08	7.06	0.0118

Table 1 represents the crystallite sizes of pure SnO₂, pure Al₂O₃ and SnO₂/Al₂O₃ films, respectively. The difference between the crystallite sizes calculated by the Scherrer formula and W-H plot indicates that all films undergo an increase in their crystallite size with some

positive value of lattice strain i.e. crystallites of all films expand during hot air annealing at 80⁰. In our work, we obtain the highest crystallite size for pure SnO₂ film, which is 11 nm according to the W-H plot. However, Al₂O₃ film possesses a lower size of crystallite with a value of 1.24 nm (W-H plot). In general, high-temperature annealing speeds up atom migration into the Al₂O₃ structure by increasing atom diffusion rates. Therefore, an increased diffusion rate produces an environment that is favourable to the formation of larger and more organised crystallites. In addition to this, Al₂O₃ may exist in a variety of phases, the most stable of which being α-Al₂O₃. This α-Al₂O₃ crystal structure is hexagonal. An increase in temperature accelerates the phase change process, resulting in α-phases with bigger crystallite sizes. In our case, due to the low-temperature annealing diffusion rate of atoms into the Al₂O₃ structure is not much high, resulting in a slow phase transformation process of Al₂O₃. Therefore, we can say that the low-temperature annealing process hinders the growth of Al₂O₃ crystallites in our films. Moreover, it is noticeable that composite SnO₂/Al₂O₃ film possesses a crystallite size which is lower than the crystallite size of pure SnO₂. The decrease in crystallite size for the composite film can assign to the fact that the addition of an Al₂O₃ into SnO₂ prevents crystallite growth during the hot air annealing process. The addition of Al₂O₃ reduces the grain size of SnO₂. Al₂O₃, generally, inhibits the SnO₂ crystallite growth due to the segregation on the surface of the SnO₂ [52]. Therefore, due to the interaction between the surfaces of the SnO₂ and Al₂O₃ and the reduction of diffusion rates, we obtain a relatively low crystallite size for SnO₂/Al₂O₃ film when compared to pure SnO₂ film.

In SnO₂/Al₂O₃ films, the presence of an amorphous phase alongside the crystalline phase, often resulting from lower annealing temperatures, significantly enhances the

material's optical and electrical properties [53]. The amorphous phase reduces grain boundary defects and scattering, facilitating improved charge carrier mobility and minimizing recombination losses [54]. It also broadens localized states near the band edges, potentially reducing the effective bandgap and increasing light absorption [55]. Additionally, the amorphous regions enhance internal light scattering, extending the optical path length and improving photocatalytic efficiency [56]. Furthermore, the smoother surface and structural flexibility provided by the amorphous phase stabilize the crystalline regions, ensuring better interaction with reactant molecules and improved thermal stability [57]. This synergistic interplay between amorphous and crystalline phases is crucial for achieving enhanced functionality in SnO_2/Al_2O_3 films.

Field emission scanning electron microscope (FESEM) images are captured and displayed in Fig. 2 (d), (e), (f) and (g) respectively, to analyse the morphology of our spin-coated films. Every image clearly illustrates the homogenous dispersion of particles within the film area. The low-resolution FESEM images of pure SnO_2 and Al_2O_3 films are depicted in Fig. 2 (d) and (e). In both films, the particles are spherical and uniformly distributed. Fig. 2 (f) and (g) represent low and high-resolution FESEM images of the SnO_2/Al_2O_3 composite film, respectively. The high-resolution images shown in Fig. 2 (h) & (i) clearly demonstrate the formation of SnO_2/Al_2O_3 nanoflower structure over the glass substrate. Moreover, the homogeneous dispersion of nanoparticles can be clearly observed in both images.

To get critical information about the functional groups of SnO_2, Al_2O_3, and SnO_2/Al_2O_3 spin-coated films, the FTIR spectra are recorded in transmittance mode. The FTIR spectra of all films are shown in Fig. 2 (j). The broad peak at 3200 cm^{-1} can be attributed to the stretching vibration of O-H groups in all three films. The strength of this peak is observed to be highest in Al_2O_3 films and lowest in SnO_2/Al_2O_3 films. Furthermore, bending vibrations of the O-H group are responsible for peaks of about 1630 cm^{-1} in all three films [47]. In this portion, SnO_2 film exhibits maximum intensity. The peaks around 2200 cm^{-1} are observed due to instrumental error. In the fingerprint region, a peak around 500 cm^{-1} of pure SnO_2 and SnO_2/Al_2O_3 film can be assigned to the stretching vibration of Sn-O or O-Sn-O [51]. The strength of this peak drastically decreases for SnO_2/Al_2O_3 films, as seen in Fig. 2 (j). This decrease in metal-oxygen vibrations can be attributed to Sn or O vacancy in the SnO_2/Al_2O_3 film. Similarly, peaks around 650 cm^{-1}, 1100 cm^{-1}, and 1450 cm^{-1}

^{1} found in pure Al_2O_3 and SnO_2/Al_2O_3 films are mostly due to Al-O and O-Al-O stretching vibrations [58]. Following the same pattern, the strength of these peaks decreases in SnO_2/Al_2O_3, showing the lack of Al or O in the SnO_2/Al_2O_3 film. In general, the vacancy of Sn, Al, or O can result in the presence of a weak stretching metal-oxygen bond in a SnO_2/Al_2O_3 film. Furthermore, the occurrence of several weak vibrations rather than one strong vibration is indicated by the widening of these peaks in SnO_2/Al_2O_3 films [47, 51]. As a result, the FTIR spectra of our films reveal that the SnO_2/Al_2O_3 film has the highest number of Sn, Al, or O vacancies than the other two films. Because the films are dried in a hot air oven, which is an oxygen-sufficient environment, the possibility of O vacancies is quite low. Furthermore, for SnO_2/Al_2O_3 films, the lowering of peak intensities associated with metal-oxygen vibrations is greater for Sn-O vibrations rather than Al-O vibrations. This phenomenon implies that Sn will most likely be replaced by Al in the aforementioned film.

4.2. Study of optical properties

Fig. 3 (a), (b) and (c) illustrates the UV-Visible absorbance, transmittance, and reflectance spectra of spin-coated films to determine their optical properties. According to Fig. 3 (a), SnO_2/Al_2O_3 film exhibits maximum absorbance in the entire UV and visible regions when compared with pure SnO_2 and Al_2O_3 films. These three films have relatively higher absorbance in the UV region, and their absorbance value decreases as wavelength increases in the visible region. SnO_2/Al_2O_3 film attains maximum absorbance at 327 nm with a secondary absorbance peak at 344 nm, respectively. Generally, in a metal-oxide composite, such peaks arise as a result of inter-band transitions between the two metal oxides [59]. Pure SnO_2 film shows maximum absorbance around 300 nm with a single absorbance peak meanwhile, pure Al_2O_3 film exhibits maximum absorbance at 319 nm with a secondary peak at 353 nm, respectively. From Fig. 3 (a), it is clear that the main absorbance peak of SnO_2/Al_2O_3 film is slightly red-shifted. This occurrence of 'red shift' in the absorbance of SnO_2/Al_2O_3 film can be attributed to the change in band gap as a result of the composite structure of pure SnO_2 and Al_2O_3, respectively. The peak positions of absorbance spectra of all samples are depicted in the inset figure of Fig. 3 (a) respectively.
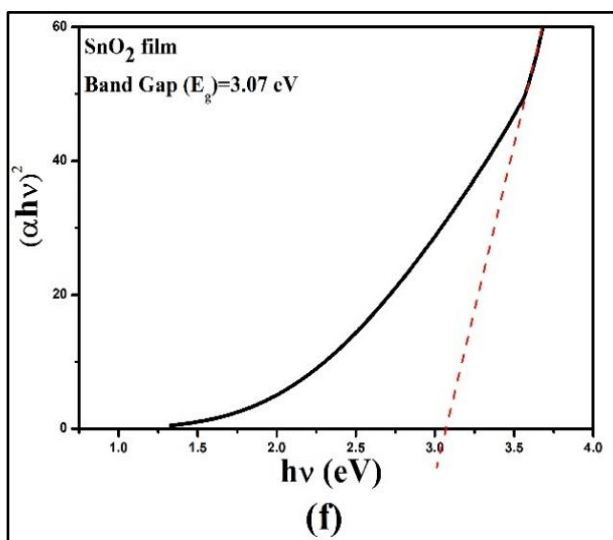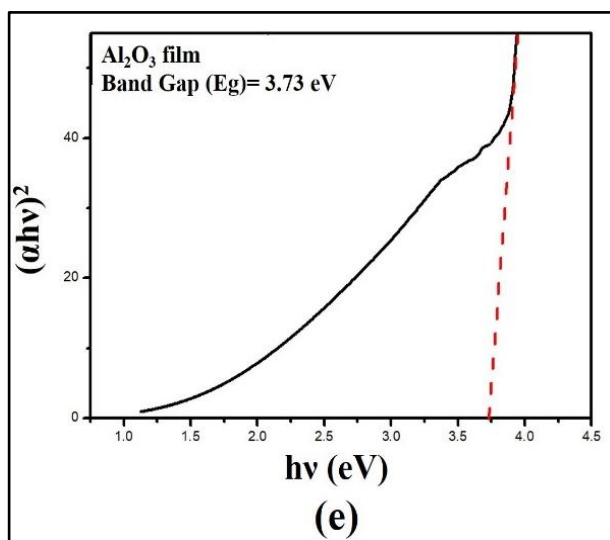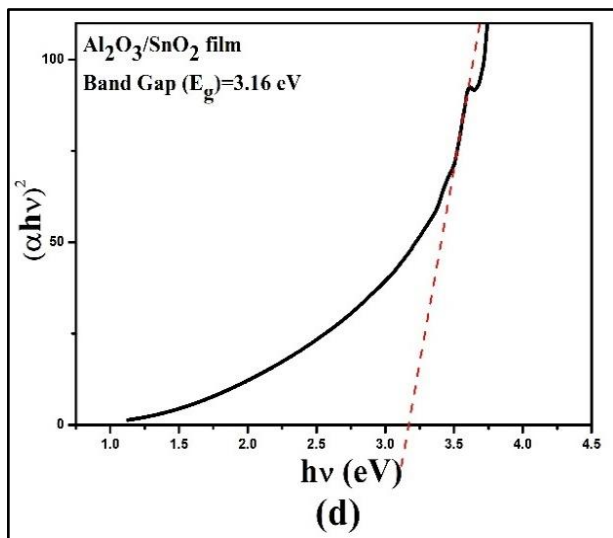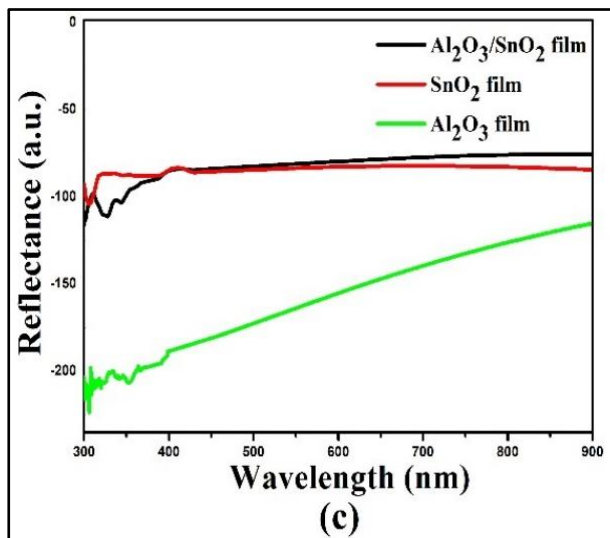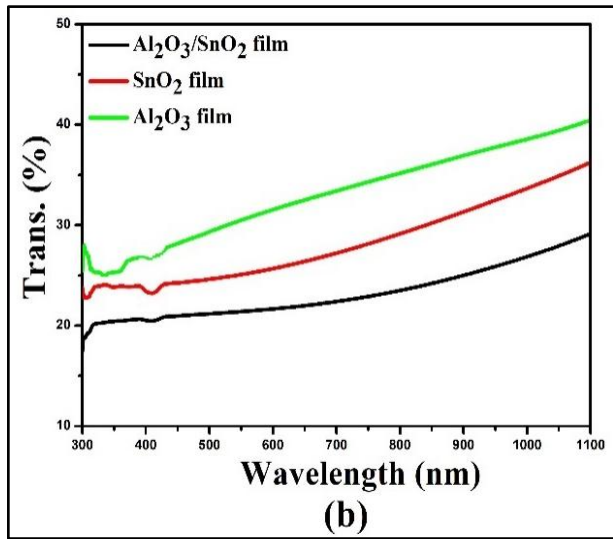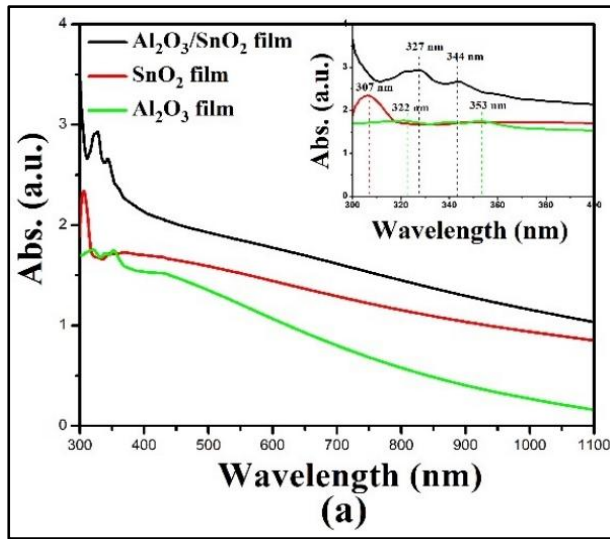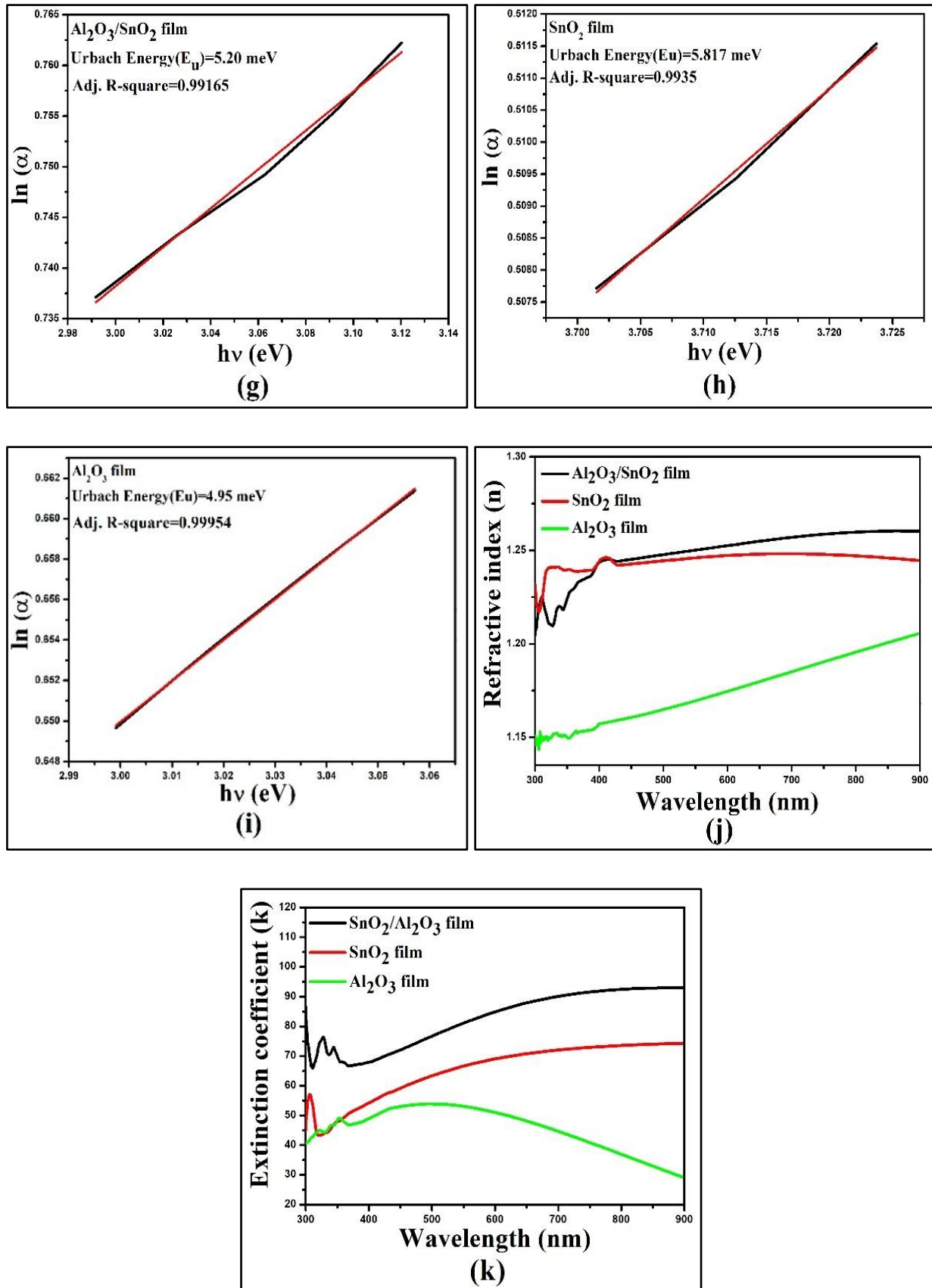
Fig. 3. UV-Visible (a) Absorbance (inset: absorbance peak position within the 300-400 nm wavelength range), (b) Transmittance and (c) Reflectance spectra of all spin coated films. Determination of Optical band gap of (d) SnO_2/Al_2O_3, (e) Al_2O_3, (f) SnO_2 films by Tauc's plot. Plot of 'ln α' versus 'hv' for the calculation of Urbach energy for (g) SnO_2/Al_2O_3, (h) SnO_2, (i) Al_2O_3 films. (j) Refractive index as a function of incident photon wavelength (k) extinction coefficient as a function of incident photon wavelength (colour online)

Variations of transmittance values with wavelength for all three films are presented in Fig. 3 (b). It is clear that all films exhibit relatively low transmittance which is below 40%. The lowest value of transmittance is observed for SnO$_2$/Al$_2$O$_3$ film which is around 20% in the UV region and its value varies between 20 to 25% in the visible regions. In the visible range, a relatively higher percentage of transmittance is observed for Al$_2$O$_3$ film (32% to 40%). Values of reflectance for all the spin-coated films are also presented in Fig. 3 (c). It is clearly seen from Fig. 3 (c) that pure Al$_2$O$_3$ minimum exhibits low reflectance compared to the other two films. SnO$_2$/Al$_2$O$_3$ film shows relatively low reflectance values in the UV region than that of pure SnO$_2$ films but in the visible region, their reflectance values are relatively same.

To calculate the thickness (t) of all the sample films prepared using the spin coating technique, we are using the relation given in equation (2),

$$t = \frac{\lambda_1 \lambda_2}{2(\lambda_1 n_2 - \lambda_2 n_1)} \qquad (2)$$

where, n_1 and n_2 are refractive indices of the film corresponding to wavelength λ_1 and λ_2, respectively [60]. Refractive indices n_1 and n_2 are calculated by using the equation (3).

$$n_{1(2)} = \left[N_{1(2)} + \left(N^2_{1(2)} - S^2\right)^{\frac{1}{2}}\right]^{\frac{1}{2}} \qquad (3)$$

In this equation, 'S' represents the refractive index of the substrate material, which is a glass slide in our work. The refractive index of this glass slide is 1.52. Here, $N_{1(2)}$ represents the order of interference [60, 61], which can be obtained from the equation (4).

$$N_{1(2)} = \frac{2S(T_{M1(2)} - T_m)}{T_{M1(2)}T_m} + \frac{(S^2 + 1)}{2} \qquad (4)$$

Here, $T_{M1(2)}$ are the values of maximum transmittance at wavelengths λ_1 and λ_2, respectively. T_m represents the minimum value transmittance value which is confined in between T_{M1} and T_{M2}. All the calculated values of thickness are listed in Table 2. Various kinds of literature have reported that the thickness of a spin-coated film depends upon various factors such that a number of layers [62], concentration of the precursor used [63], rotation per minute of the spin coating [64] and drying temperature [65]. In our case, the thickness of the prepared films is also affected by the viscosity of the sol-gel solution used. Many researchers have reported that a good-quality spin-coated film has a thickness around 300 nm [66, 67]. Generally, high temperature annealing increases the density of film which results in a reduction of the deposited film thickness but, in our case, the drying temperature is not that high (only 80 ºC). So, we have obtained a relatively high thickness, which is more than the standard value, for our spin-coated films [68].

The optical band gap in a solid-state material is the most minimal amount of energy required for an electron to move from the valence band to the conduction band. Electronic characteristics of a material, especially in the context of semiconductors, are greatly influenced by the optical band gap. Designing materials with certain functionality, such as those used in solar cells, LEDs, and photodetectors, depends on understanding these energy gaps. In our work, optical bandgaps of all the spin-coated films are examined by calculating the values of absorbance coefficient (α). The equation (5) is used to calculate the absorbance coefficient (α) that involves film thickness and transmittance data [69].

$$\alpha = \frac{1}{t}\ln\left(\frac{1}{T}\right) \qquad (5)$$

where, 't' is the film thickness and 'T' is the transmittance. Here, we are calculating the values of direct optical band gap (n=2) using Tauc's plot. The Tauc's relation [70] can be written as,

$$(\alpha h\nu)^2 = A\left(h\nu - E_g\right) \qquad (6)$$

Here, hν is incident photon energy, E$_g$ is the direct bandgap value and A is absorbance. For the calculation of the direct optical band gap, we plot 'hν' as X-axis and $(\alpha h\nu)^2$ as Y-axis, respectively. The intersection by the extrapolation of the first linear part of the above plot at the X-axis gives the value of the direct optical band gap of our films. Table 2 shows the values and Fig. 3 (d), (e) and (f) present the Tauc's plot of the direct optical band gap of SnO$_2$/Al$_2$O$_3$, pure Al$_2$O$_3$ and pure SnO$_2$ films. From Fig. 3 (f), it is clear that pure SnO$_2$ film exhibits a lower band gap (3.07 eV), while, that of pure Al$_2$O$_3$ film is quite high (Fig. 3 (e)). However, its value decreases for the composite SnO$_2$/Al$_2$O$_3$ film. This reduction of bandgap can be attributed to the introduction of SnO$_2$ into the Al$_2$O$_3$ nanosystem. Formation of different types of energy states during the drying process of SnO$_2$/Al$_2$O$_3$ is mainly responsible for such reduction of the bandgap.

By calculating Urbach energy, it is possible to validate the existence of defect levels, also known as localized electronic energy states within the forbidden energy gap of a semiconducting material. Urbach energy is a very noteworthy parameter, since, it serves as an indicator for the width of the localized energy tail just below the conduction band and above the valence band. These band tail states are characterized by Urbach energy with an exponential distribution [47, 71, 72]. For incident photon having energy 'hν', the relation between 'α' and Urbach energy (E$_u$) of a material [73] can be established by the equation (7),

$$\alpha = \alpha_0 \exp(h\nu/Eu) \qquad (7)$$

The values of Urbach energy are calculated from the plot 'ln α' versus 'hν', which exhibits linear nature near the fundamental band edge. The reciprocal of the slope of this part represents the value of Urbach energy [47]. Fig. 3 (g), (h) and (i) represent the plots of Urbach energy for SnO$_2$/Al$_2$O$_3$, pure SnO$_2$ and pure Al$_2$O$_3$ films respectively.

Their Urbach energy values are displayed in Table 2. The highest value of Urbach energy of pure SnO₂ film can be attributed to the higher density of defect-introduced energy levels. This fact is also supported by the calculation of the band gap using Tauc's plot. Relatively high Urbach energy of SnO₂ film leads to the lower band gap value as a result of introducing defect levels. However, pure Al₂O₃ film shows a lower Urbach energy value. This signifies that pure Al₂O₃ film has a lower defect density than the other two films. High crystallinity and defect-free nature are indicated by higher band gap as well as lower Urbach energy values for pure Al₂O₃ film. SnO₂/Al₂O₃ composite film exhibits a lower Urbach energy value than that of pure SnO₂ and higher than pure Al₂O₃ film. Here, we can conclude that the introduction of SnO₂ into Al₂O₃ increases the defect levels and compositional disorder. Lattice distortion and oxygen vacancies are likely to occur due to heat treatment and may introduce localized energy levels in SnO₂/Al₂O₃ film. So, we obtain a lower optical band gap and higher Urbach energy for SnO₂/Al₂O₃ film when compared to pure Al₂O₃ film.

The refractive index is a very significant parameter that determines the potential of an optical material in various practical domains. The refractive index(n′) of a material is a complex parameter having a real part(n) known as the linear refractive index and an imaginary part(k) known as the extinction coefficient [74, 75]. Therefore, the refractive index can be written as-

$$\text{n}' = \text{n} + \text{i}\text{k} \tag{8}$$

For the wavelengths around the absorption edge, the linear refractive index of an optical material can be calculated with the help of band gap (Eg) values [74, 75] by using the equation (9),

$$\frac{(\text{n}^2-1)}{(\text{n}^2+2)} = 1 - (E_g/20)^{\frac{1}{2}} \tag{9}$$

The calculated values of the linear refractive index near the absorption edge for SnO₂/Al₂O₃, pure Al₂O₃ and pure SnO₂ films are listed in Table 2. We obtain the highest refractive index 2.38 for SnO₂ films. The refractive index of Al₂O₃ and SnO₂/Al₂O₃ films are 2.22 and 2.35, respectively.

Generally, the refractive index is a wavelength-dependent parameter. The incident photon wavelength(λ) dependency of the refractive index is depicted in Fig. 3 (j). The 'n' versus 'λ' graph shown in that figure clearly demonstrates the variation of 'n' with 'λ' in both UV and visible regions. Similar to the linear refractive index, the extinction coefficient(k) is also a wavelength-dependent parameter. The change in 'k' with wavelength(λ) is displayed in Fig. 3 (k). Values of both 'n' and 'k' are calculated by using the equations (10) and (11) established by Bethe et al. [76] and Belgacem et al. [77].

$$\text{n} = \frac{1+R}{1-R} + \left(\frac{4R}{(1-R)^2} + k^2\right)^{\frac{1}{2}} \tag{10}$$

$$k = \frac{\alpha\lambda}{4\pi} \tag{11}$$

'n' versus 'λ' plot in Fig. 3 (j) clearly demonstrates that Al₂O₃ film has a lower refractive index in the entire UV and visible region than that of the SnO₂ and SnO₂/Al₂O₃ films. However, all three films show a similar trend that their 'n' values increase gradually with an increase in 'λ'. The highest refractive index in the UV region is observed for pure SnO₂ film but SnO₂/Al₂O₃ film exhibits the highest refractive index in the visible region. Vankhade et al. during the study of the effect of thickness on the optical properties of spin-coated PbS thin films found that refractive indices of the said films increase with an increase in thickness [78]. In our case, the refractive indices of all films agree well with this fact. However, the relationship between thickness and refractive index varies depending upon the material used and deposition methods that are adopted for film preparation. In addition to this, the optical band gap value also influences the refractive index of a material. Al₂O₃ is an insulator with a wide band gap, whereas, SnO₂ is a semiconductor with a lower band gap value than Al₂O₃. Ravindra et al. have reported that a higher band gap always results in a lower refractive index [79]. Our experimental result agrees well with this conclusion also. Since we have already discussed that the introduction of SnO₂ into the Al₂O₃ nano system lowers the band gap value, so, we have obtained a relatively higher refractive index for SnO₂/Al₂O₃ film than that of Al₂O₃ film.

Variations of extinction coefficient (k) with wavelength(λ) at 600 nm are listed in Table 2. Similar to the refractive index, the extinction coefficient is also band gap dependent [80]. A higher band gap always leads towards a lower extinction band gap. Moreover, a film with a higher refractive index scatters and absorbs more light within the film [81]. So, we have obtained higher 'k' values for pure SnO₂ and SnO₂/Al₂O₃ films than Al₂O₃ films.

Table 2. Values of thickness, optical band gap, Urbach energy, refractive index and extinction of our films

Name of films	Thickness (t) in nm.	Optical band gap (Eg) in eV	Urbach energy (Eu) in meV	Refractive index(n) near the absorption edge	Extinction coefficient(k) at 600 nm
SnO₂/Al₂O₃	467.78	3.16	5.20	2.35	84.99
Al₂O₃	381.26	3.73	4.95	2.22	50.96
SnO₂	433.21	3.06	5.81	2.38	68.54

4.3. Electrical characterization

A planar geometry of the device has been used in order to take the *I-V* measurement. Initially, a clean glass substrate of area 1.04 mm² has been taken followed by the

deposition of thin film of the prepared materials by drop casting method. Two metal electrodes made of silver conducting paste have been deposited on the film which are connected to the Keithley source measure unit. A schematic diagram of the device is shown in Fig. 4 (a). The *I-V* characteristics of the as-prepared pristine SnO_2, Al_2O_3 and their composite SnO_2/Al_2O_3 are taken in the voltage range of -10V to 10V as shown in Fig. 4 (b).

The *I-V* measurements are carried out with the help of a Keithley source meter (Model: Keithley 2450). The *I-V* curves as can be seen from the figure show an ohmic nature within the measured voltage range for bare SnO_2 and Al_2O_3 films whereas SnO_2/Al_2O_3 is showing a rectifying nature. This may be due to the fact that both SnO_2 and Al_2O_3 materials have comparatively higher bandgap which means that it requires a significant amount of energy to excite electrons from the valence band to the conduction band. As a result, the *I-V* characteristics of both materials show an ohmic behaviour which means that the current increases linearly with the voltage [82-84]. On the other hand, in the case of their composite SnO_2/Al_2O_3, as both the materials are combined to form the composite, their individual electronic properties can interact at the interface between the two materials which can lead to the formation of heterojunction with different energy levels, affecting the flow of charge carriers that leads to rectifying behaviour similar to diodes [85-87]. In addition to that, for bare SnO_2 and Al_2O_3, the *I-V* characteristics exhibit ohmic behaviour due to the absence of a significant energy barrier for charge carriers. However, when these materials are combined into a composite, the difference in work function between them results in the creation of a Schottky barrier at the interface which prevents the flow of charge carriers in one direction, leading to rectifying behaviour in the *I-V* curve [88-91]. Thus, this composite material can find good applicability in various optoelectronic devices such as photodiodes that needs a further investigation of the device properties based on these materials. The values of current are found from the figure as 2.74E-07A, 7.54E-07A and 8.45E-07A for SnO_2, Al_2O_3 and SnO_2/Al_2O_3 respectively at 10V bias voltage. The significant increase in current in the case of composite SnO_2/Al_2O_3 than both the SnO_2 and Al_2O_3 materials separately can be attributed to the excess carrier generation at the interface states which contributes to the conductivity of the materials [92, 93]. During the formation of composite material some interfacial states are created with the conduction band minimum and valence band maximum which supplies the excess number of external carriers that leads to the increase in conductivity of the material. Thus, this composite material is showing far improved electrical characteristics that may contribute invaluably towards future optoelectronic devices.

The SnO_2/Al_2O_3 nanocomposite system developed in this study represents a noteworthy advancement in nanostructured materials, particularly in terms of structural, optical, morphological, and electrical properties. Unlike polymer-based nanocomposites, which often depend on chemical modifiers to enhance stability and compatibility [94], our SnO_2/Al_2O_3 composites inherently exhibit robust compatibility between the constituent materials. This intrinsic synergy results in uniform and stable nanostructures with a nano-flower morphology that offers a high surface area and improved interfacial interactions, surpassing the structural integration achieved by systems like cellulose acetate (CA)@metal oxide hybrids [94]. Additionally, the synthesis approach employed here avoids the complexity typically associated with MOF-derived oxides or graphene oxide composites [95, 96], providing a simpler and scalable pathway with comparable structural advantages.
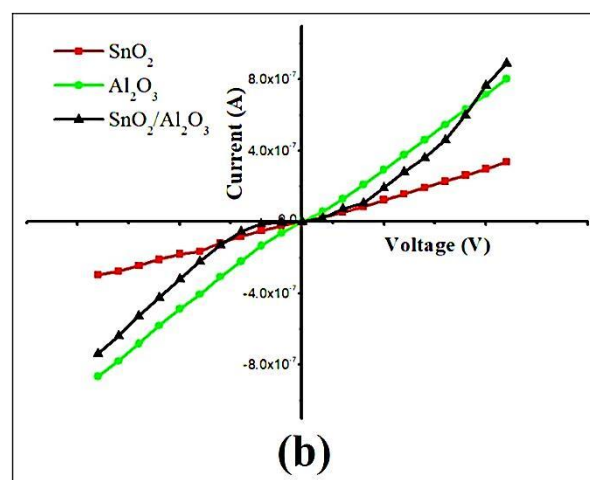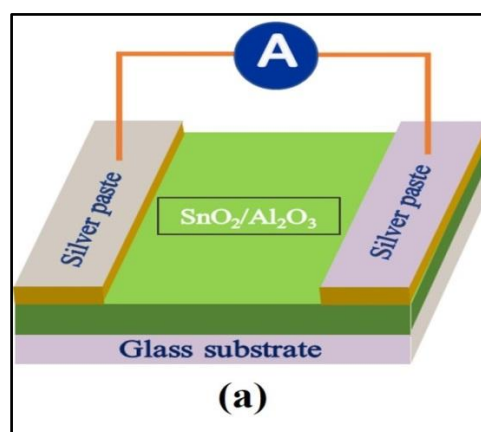

Fig. 4. (a) Schematic diagram of device structure. (b) I-V characteristics of SnO₂, Al₂O₃ and SnO₂/Al₂O₃ spin-coated films (colour online)

The optical properties of the SnO_2/Al_2O_3 system reveal exceptional light absorption, attributed to its carefully engineered electronic structure. Unlike TiO_2-GO hybrids or MXene-metal oxide systems, which require material blending or external doping to achieve band gap modifications [97, 98], our composites display naturally optimized optical properties without any external modifications. This inherent feature eliminates the need for additional tuning, making the material highly attractive for optoelectronic applications. Moreover, compared to

sodium alginate/polyvinyl alcohol-ZnO/Fe$_3$O$_4$ films that show moderate optical improvements with the incorporation of nanofillers [99], our composites achieve superior optical performance through strategic material design alone.

Electrically, the SnO$_2$/Al$_2$O$_3$ composites exhibit non-ohmic conduction, a behaviour arising from the distinctive interfacial dynamics between the two oxides. Unlike MOF-derived composites [100, 101], which rely on complex architectures to enhance charge transport, our materials achieve improved charge carrier mobility and reduced recombination solely through effective interface engineering. This eliminates the need for conductive additives or secondary phases often employed in polymer-metal oxide systems [102, 103]. Such enhancements make our composites strong contenders for energy storage applications, rivalling the performance of MXene-based hybrids, which similarly leverage interfacial interactions to boost transport properties [104].

Morphologically, the unique nano-flower structure of our films sets them apart from other systems. For instance, ZnO/Fe$_3$O$_4$-polymer systems generally exhibit spherical or rod-like nanostructures [105], which lack the interfacial synergy provided by our composite's well-defined morphology. This enhanced morphology directly contributes to the improved optical and electrical properties, outperforming the functional characteristics of MOF-derived or polymer-based composites [100, 101, 106, 107].

When considered for electronic applications, the SnO$_2$/Al$_2$O$_3$ composites address critical challenges related to stability, scalability, and multifunctionality. For example, polypyrrole-metal oxide systems designed for electromagnetic interference shielding rely on intrinsic conductivity and relaxation effects [108], while our composites achieve similar multifunctionality through precise interface engineering and morphological control. This structural stability and versatility align with the requirements for next-generation electronic materials.

Furthermore, our work provides valuable insights into the development of advanced humidity sensors based on semiconductor metal oxides [109]. Whereas traditional SMO-based composites often face limitations in achieving optimal sensitivity and dynamic range, the tailored morphology and interfacial properties of our materials offer a promising foundation for sensor applications. Additionally, the high surface area and superior electrical properties of our composites position them as excellent candidates for supercapacitors, paralleling the performance of MOF-derived systems [106, 107].

In conclusion, the SnO$_2$/Al$_2$O$_3$ nanocomposites developed here represent a holistic solution for achieving structural stability, enhanced optical properties, and superior electrical performance. By addressing the inherent limitations of polymer-based hybrids, MOF-derived materials, and graphene oxide composites, this study establishes a new benchmark for multifunctional nanocomposites, offering a versatile platform for advancements in cutting-edge material research.

5. Conclusions

In our study, three thin films of pure SnO$_2$, pure Al$_2$O$_3$, and SnO$_2$/Al$_2$O$_3$ composites are synthesised using a sol-gel-aided spin-coating process. Even though all films are synthesised under similar drying conditions, the SnO$_2$/Al$_2$O$_3$ film possesses the maximum thickness (467.78 nm). UV-Visible absorbance investigations reveal that SnO$_2$/Al$_2$O$_3$ films have a slightly wider bandgap than pure SnO$_2$ films and a lower bandgap value than pure Al$_2$O$_3$ films. In addition, Urbach energy calculations show that SnO$_2$/Al$_2$O$_3$ films have a greater Urbach energy value than pure Al$_2$O$_3$ films. The generation of localised energy states in the forbidden region as a result of heterostructure formation between SnO$_2$ and Al$_2$O$_3$ is indicated by the higher Urbach energy value of the SnO$_2$/Al$_2$O$_3$ film. In addition, optical property analysis reveals that the SnO$_2$/Al$_2$O$_3$ film has a greater extinction coefficient and refractive index than the other two pure films. The XRD spectra of our films demonstrate that pure SnO$_2$ film has the largest crystallite size and pure Al$_2$O$_3$ film has the smallest crystallite size under both Scherrer and W-H plot approaches. However, SnO$_2$/Al$_2$O$_3$ film has an intermediate crystallite size that is higher than pure Al$_2$O$_3$ and lower than pure SnO$_2$ films. SEM images of SnO$_2$/Al$_2$O$_3$ film clearly illustrate the formation of nanoflower structure of SnO$_2$/Al$_2$O$_3$ composite. FTIR analysis of all films reveals that the intensities of metal-oxygen bond vibrations are reduced for SnO$_2$/Al$_2$O$_3$ film when compared to pure SnO$_2$ and Al$_2$O$_3$ films. After knowing the properties of these films, we investigated their I-V characteristics. An investigation of the I-V properties of our films shows exceptional behaviour displayed by SnO$_2$/Al$_2$O$_3$. This film exhibits a non-ohmic nature whereas the other two films of pure SnO$_2$ and Al$_2$O$_3$ manifest an ohmic nature within the voltage range of -10V to 10V. Due to its exceptional electronic behaviour, SnO$_2$/Al$_2$O$_3$ nanoflower composites have a high potential as synthesis materials for different optoelectronic applications.

References

[1] T. W. Hamann, R. A. Jensen, A. B. Martinson, H. Van Ryswyk, J. T. Hupp, Energy Environ. Sci. **1**(1), 66 (2008).
[2] M. Kesavan, V. Sannasi, M. Kathiresan, M. Ramesh,

Bull. Mater. Sci. **46**(2), 90 (2023).

[3] H. Dalal, M. Kumar, S. Devi, P. Sehrawat, M. Sheoran, P. Devi, N. Sehrawat, R. K. Malik, Bull. Mater. Sci. **46**(3), 173 (2023).

[4] T. Xie, G. Liu, B. Wen, J. Y. Ha, N. V. Nguyen, A. Motayed, R. Debnath, ACS Appl. Mater. Interfaces **7**(18), 9660 (2015).

[5] K. Lê, N. Heshmati, S. Mathur, Nano Convergence **10**(1), 47 (2023).

[6] J. Pak, K. Cho, J. K. Kim, Y. Jang, J. Shin, J. Kim, J. Seo, S. Chung, T. Lee, Nano Futures **3**(1), 011002 (2019).

[7] H. W. Lee, S. Kim, J. Kim, E. Kim, J. Korean Phys. Soc. **82**(3), 280 (2023).

[8] J. Jeon, Y. Ha, J. L. MacManus-Driscoll, S. Lee, Nano Convergence **10**(1), 50 (2023).

[9] R. Mahanta, P. Chetri, N. Parasar, D. Neog, B. Mohanta, J. Korean Phys. Soc. 1 (2024).

[10] H. J. Kim, M. J. Maeng, J. H. Park, M. G. Kang, C. Y. Kang, Y. Park, Y. J. Chang, Current Appl. Phys. **19**(2), 168 (2019).

[11] J. H. Kwon, S. Jang, H. J. Kim, B. S. Joo, K. N. Yu, E. Choi, Y. S. Jeong, Y. Park, Y. J. Chang, J. Anal. Sci. Technol. **11**, 1 (2020).

[12] D. Lee, D. Bae, M. Chae, H. D. Kim, J. Korean Phys. Soc. **80**(11), 1065 (2022).

[13] R. Mahanta, P. Chetri, D. Bora, Physica Scripta **98**(11), 115955 (2023).

[14] P. Wu, B. Zhou, W. Zhou, Appl. Phys. Lett. **100**(18), 182405 (2012).

[15] S. S. Lee, W. K. Jung, K. Lee, I. K. Park, J. Korean Phys. Soc. **82**(2), 181 (2023).

[16] D. Muchahary, L. S. Ram, R. Narzary, P. P. Sahu, S. Bhattarai, S. Tayal, Current Appl. Phys. **38**, 15 (2022).

[17] F. B. Hualpa, L. Calaza, D. Garcia, M. A. Garcia, J. A. Villegas, 239th ECS Meeting with the 18th International Meeting on Chemical Sensors (IMCS), ECS (2021).

[18] S. M. Ali, E. H. Hussein, O. A. Dakhil, Nano Futures **5**(3), 035001 (2021).

[19] P. Chetri, B. Saikia, A. Choudhury, J. Appl. Phys. **113**(23), 233514 (2013).

[20] Y. Ha, S. Lee, Nano Convergence **10**(1), 9 (2023).

[21] I. J. Park, H. K. An, Y. Chang, J. Y. Kim, Nano Convergence **10**(1), 22 (2023).

[22] L. A. Moisés, A. J. Chiquito, Current Appl. Phys. **53**, 165 (2023).

[23] H. Lee, S. B. Kang, S. Lee, K. Zhu, D. H. Kim, Nano Convergence **10**(1), 27 (2023).

[24] H. Kang, J. S. Kim, S. R. Choi, Y. H. Kim, D. H. Kim, J. G. Kim, J. H. Cho, Nano Convergence **9**, 1 (2022).

[25] L. D. S. de Oliveira, L. P. Fonseca, R. D. de Souza, C. D. F. Bueno, L. M. Martins, L. V. Scalvi, Current Appl. Phys. **41**, 49 (2022).

[26] N. Siregar, J. H. Panggabean, J. Phys.: Conf. Ser. **1819**(1), 012032 (2021).

[27] S. A. Adewinbi, J. A. Akinmoladun, M. A. Olaniyan, M. O. Akinmoladun, M. A. Adeyemi, M.

T. B. Dauda, J. Mater. Chem. Phys. **264**, 124468 (2021).

[28] Y. S. Uday, H. C. Manjunatha, Y. S. Vidya, S. Manjunatha, R. Soundar, K. N. Sridhar, Current Appl. Phys. **55**, 9 (2023).

[29] B. C. Anand, R. Shashidhar, N. Choudhary, J. Korean Phys. Soc. **82**(4), 392 (2023).

[30] N. Houaidji, K. Malek, M. A. Ouaissa, M. A. Boubekri, M. S. T. Messaoudi, Optik **208**, 164026 (2020).

[31] K. C. Lee, M. J. Jeong, S. W. Wi, M. C. Choi, S. Y. Park, F. H. Naqvi, Y. S. Lee, Current Appl. Phys. **56**, 1 (2023).

[32] R. A. Zargar, M. S. Ali, N. A. Shahid, M. S. Siddiqui, S. Ali, S. S. Khan, Optik **127**(17), 6997 (2016).

[33] H. Guendouz, A. Bouaine, N. Brihi, Optik **158**, 1342 (2018).

[34] K. Verma, B. Chaudhary, V. Kumar, A. Agrawal, R. Srivastava, Vacuum **146**, 478 (2017).

[35] G. K. Dalapati, H. Sharma, A. Guchhait, N. Chakrabarty, P. Bamola, Q. Liu, G. Saianand, A. M. S. Krishna, S. Mukhopadhyay, A. Dey, T. K. S. Wong, S. Zhuk, S. Ghosh, S. Chakrabortty, C. Mahata, S. Biring, A. Kumar, C. S. Ribeiro, S. Ramakrishna, A. K. Chakraborty, S. Krishnamurthy, P. Sonar, M. Sharma, J. Mater. Chem. A **9**(31), 16621 (2021).

[36] M. Al-Gharram, F. Al-Khaled, H. Al-Tarazi, Surfaces Interfaces **52**, 104939 (2024).

[37] J. E. Medvedeva, Transparent Electronics: From Synthesis to Applications **29**, (2010).

[38] C. Zhan, W. Sun, D. Pan, Z. Li, J. Mater. Chem. C **5**(7), 1569 (2017).

[39] X. Yu, T. J. Marks, A. Facchetti, Nat. Mater. **15**(4), 383 (2016).

[40] D. S. Chormey, E. K. Gbadam, N. Amponsah, Environ. Chem. Lett. **21**(3), 1863 (2023).

[41] G. Korotcenkov, Chem. Sensors **1**, 313 (2010).

[42] R. Yang, Z. Wang, Y. Liang, Nano Energy **83**, 105849 (2021).

[43] P. Boryło, M. Kaczmarek, J. Nowicki, J. Patkowski, Vacuum **131**, 319 (2016).

[44] A. Faraji, F. Alamouti, A. Singh, K. K. Gupta, J. Asian Ceram. Soc. **9**(1), 366 (2021).

[45] M. L. Dieuzeide, A. Segura, M. Miranda, M. A. Garcia, R. Argueta, Int. J. Hydrogen Energy **41**(1), 157 (2016).

[46] P. Chetri, A. Choudhury, Physica E **47**, 257 (2013).

[47] R. Mahanta, P. Chetri, N. Shukla, D. Bora, Physica B: Condensed Matter **690**(1), 416230 (2024).

[48] D. P. Birnie III, Sol-gel Technol. Glass Producers Users **1**, 49 (2004).

[49] M. D. Tyona, Advances Mater. Res. **2**(4), 181 (2013).

[50] G. Jacopin, L. Xu, M. Yang, Nanotechnology **23**(32), 325701 (2012).

[51] P. Chetri, B. Saikia, A. Choudhury, J. Appl. Phys. **113**(23), 233514 (2013).

[52] Z. K. Heiba, N. G. Imam, M. B. Mohamed, J. Mol.

Struct. **1115**, 156 (2016).

[53] M. A. Sayeed, H. K. Rouf, J. Mater. Res. Technol. **15**, 3409 (2021).

[54] B. Wang, Y. Zhao, X. Lin, D. Li, Chem. Soc. Rev. **50**(12), 6914 (2021).

[55] M. Imran, A. Ali, N. Ahmed, Thin Solid Films **648**, 31 (2018).

[56] S. Sun, F. Liu, X. Zhang, Catal. Sci. Technol. **9**(16), 4198 (2019).

[57] J. Kang, Q. Wang, C. Zhang, Chem. Rev. **123**(13), 8859 (2023).

[58] V. P. Dhawale, V. Khobragade, S. D. Kulkarni, Chemistry **27**, 31 (2018).

[59] M. Zhang, X. Yang, G. Zhang, J. Applied Catal. A: Gen. **260**(2), 215 (2004).

[60] R. Swanepoel, J. Phys. E: Sci. Instrum. **16**, 1214 (1983).

[61] F. Carreho, J. C. Martinez-Antrh, E. Bernabeu, Rev. Sci. Instrum. **65**(8), 2489 (1994).

[62] L. Znaidi, M. J. Sayah, J. M. Guigner, M. Eddrief, L. Diaconeasa, S. Mohammadi, J. Phys. Chem. Solids **65**, 1121 (2004).

[63] M. Dutta, S. Mridha, D. Basak, Appl. Surf. Sci. **254**(1), 2743 (2008).

[64] Y. Ohya, H. Saiki, T. Tanaka, Y. Takahashi, J. Am. Ceram. Soc. **79**(9), 825 (1996).

[65] M. P. Bole, D. S. Patil, J. Phys. Chem. Solids **70**(5), 466 (2009).

[66] M. Sharma, R. M. Mehra, Appl. Surf. Sci. **255**(8), 2527 (2008).

[67] S. Mridha, D. Basak, Mater. Res. Bull. **42**(7), 875 (2007).

[68] Q. X. Jia, S. R. Foltyn, P. N. Arendt, J. F. Smith, Appl. Phys. Lett. **80**(9), 1601 (2002).

[69] G. I. Rusu, M. E. Popa, G. G. Rusu, I. Salaoru, Appl. Surf. Sci. **218**(1), 222 (2003).

[70] R. Mahanta, P. Chetri, D. Bora, Mater. Today: Proc. **19**, 67 (2023).

[71] T. S. Soliman, S. A. Vshivkov, J. Non-Cryst. Solids **519**, 119452 (2019).

[72] R. J. Sengwa, S. Choudhary, J. Alloys Compd. **701**(1), 652 (2017).

[73] S. Ilican, Y. Caglar, M. Caglar, J. Optoelectron. Adv. M. **10**(10), 2578 (2008).

[74] E. M. Abdelrazek, A. M. Abdelghany, S. I. Badr, M. A. Morsi, J. Mater. Res. Technol. **7**(1), 419 (2018).

[75] A. M. Abdelghany, E. M. Abdelrazek, S. I. Badr, M. A. Morsi, Mater. Des. **97**, 532 (2016).

[76] S. R. Bathe, P. S. Patil, Sol. Energy Mater. Sol. Cells **91**(10), 1097 (2007).

[77] S. Belgacem, R. Bennaceur, Rev. Phys. Appl. **25**(12), 1245 (1990).

[78] D. Vankhade, T. K. Chaudhuri, Opt. Mater. **98**, 109491 (2019).

[79] C. Rameshkumar, AIP Conf. Proc. **2341**(1), 1 (2021).

[80] S. Shi, J. Zhang, F. Sun, Adv. Condensed Matter Phys. **2018**, 1 (2018).

[81] M. Ghemid, H. Saikia, T. Choudhury, Chem. Phys. Lett. **784**, 139089 (2021).

[82] M. A. Sayeed, H. K. Rouf, J. Mater. Res. Technol. **15**, 3409 (2021).

[83] A. E. Delahoy, S. Guo, Handbook Photovoltaics Science and Engineering, Second Edition, John Wiley & Sons, Ltd, 716 (2011).

[84] D. Li, X. Fang, Z. Deng, S. Zhou, R. Tao, W. Dong, X. Zhu, J. Phys. D: Appl. Phys. **40**(16), 4910 (2007).

[85] K. Tennakone, V. P. S. Perera, I. R. M. Kottegoda, L. A. A. De Silva, G. R. R. A. Kumara, A. Konno, J. Electron. Mater. **30**, 992 (2001).

[86] J. Dagar, S. Castro-Hermosa, G. Lucarelli, A. Zampetti, F. Cacialli, T. M. Brown, IEEE J. Photovoltaics **9**(5), 139 (2019).

[87] S. Ying, Z. Ma, Z. Zhou, R. Tao, K. Yan, M. Xin, Y. Shi, IEEE Access **8**, 189646 (2020).

[88] Y. Xu, C. Cheng, S. Du, J. Yang, B. Yu, J. Luo, X. Duan, ACS Nano **10**(5), 4895 (2016).

[89] Y. Liu, J. Guo, E. Zhu, L. Liao, S. J. Lee, M. Ding, X. Duan, Nature **557**(7707), 696 (2018).

[90] R. T. Tung, Appl. Phys. Rev. **1**(1), 011304 (2014).

[91] J. Yu, W. Han, A. A. Suleiman, S. Han, N. Miao, F. C. C. Ling, Small Methods **7**, 2301282 (2023).

[92] Y. Pei, A. F. May, G. J. Snyder, Adv. Energy Mater. **1**(2), 291 (2011).

[93] M. Muscetta, R. Andreozzi, L. Clarizia, I. Di Somma, R. Marotta, Int. J. Hydrogen Energy **45**(53), 28531 (2020).

[94] R. S. Devan, R. A. Patil, J. H. Lin, Y. R. Ma, Adv. Funct. Mater. **22**(16), 3326 (2012).

[95] J. G. Lu, P. Chang, Z. Fan, Mater. Sci. Eng. R. Rep. **52**(1-3), 49 (2006).

[96] M. Zhi, C. Xiang, J. Li, J. Mater. Chem. **5**(1), 72 (2013).

[97] E. Comini, C. Baratto, G. Faglia, Prog. Mater. Sci. **54**(1), 1 (2009).

[98] T. He, J. Yao, Prog. Mater. Sci. **51**(6), 810 (2006).

[99] P. Karthik, J. Rajesh, S. Ravichandran, J. Water Process Eng. **66**, 106010 (2024).

[100] A. A. Bhoite, P. Pujari, A. Kulkarni, J. Energy Storage **72**, 108557 (2023).

[101] W. Zhou, Y. Zhang, F. Wang, Coord. Chem. Rev. **477**, 214949 (2023).

[102] Z. S. Wu, X. Feng, W. Ren, Nano Energy **1**(1), 107 (2012).

[103] J. Bouclé, P. Ravirajan, J. Nelson, J. Mater. Chem. **17**(30), 3141 (2007).

[104] S. Hussain, M. A. Khan, A. Afaq, Nanoscale **15**(16), 7329 (2023).

[105] I. Madaci, Université Paris-Saclay Dissertation, 2023.

[106] F. Parsapour, M. Jafari, A. Eslamian, J. Energy Storage **82**, 110487 (2024).

[107] Z. Zhang, H. Li, Y. Li, J. Energy Chem. **60**, 259 (2021).

[108] Y. Sood, M. Mudila, P. Chamoli, P. Saini, A. Kumar, Mater. Horiz. **11**, 4256 (2024).

[109] A. Kumar, S. Thakur, P. Sharma, Mater. Res. Bull. **158**, 112053 (2023).

*Corresponding address: chetripawan2009@gmail.com